INORGANIC CHEMISTRY FRONTIERS

RESEARCH ARTICLE

View Article Online
View Journal | View Issue

Cite this: *Inorg. Chem. Front.*, 2024, **11**, 1607

Synthesis of lanthanide-based scintillator@MOF nanocomposites for X-ray-induced photodynamic therapy†

Lantian Zhang,[a] Fan Gao,[a] Shiqi Liu,[a] Mei Ju,[c] Chao Sun,[d] Gengzhi Sun,[a] Qiang Ju,*[a] Kai Yang*[b] and Zhenlan Fang*[a]

Received 8th November 2023,
Accepted 22nd January 2024

DOI: 10.1039/d3qi02301j

rsc.li/frontiers-inorganic

Multifunctional nanocomposites comprising a set of diverse nanoparticles are highly desirable for realizing on-demand therapy with minimized adverse effects. X-ray-induced photodynamic therapy (X-PDT) has reformed conventional PDT for deep-seated tumors by using penetrating X-rays, but its application faces the challenge of efficiently integrating scintillators with photosensitizers. In this study, core–shell nanocomposites rationally integrating $NaGdF_4$:Tb@$NaGdF_4$:Ce@$NaLuF_4$ nanoparticles with Hf-porphyrin metal–organic frameworks (MOFs) using a surface-assisted epitaxial growth strategy have been proposed and synthesized. Herein, $NaGdF_4$:Tb@$NaGdF_4$:Ce@$NaLuF_4$ nanoparticles demonstrate strong X-ray attenuation and bright green light emissions, serving as efficient scintillators to activate the photosensitizer. The porphyrin in MOFs can absorb and be further activated by the emission of a lanthanide-based scintillator, playing the role of a photosensitizer to generate a significant amount of singlet oxygen. Moreover, uniform nanocomposites with regular core–shell structures enable the maximization of energy transfer between the scintillator and MOFs, and the inherent pores of MOFs facilitate the diffusion of reactive oxygen species (ROS) out of the interior to boost PDT efficacy. In addition, the existence of heavy atoms such as Gd, Lu, and Hf can significantly enhance radiation sensitization, facilitating the production of hydroxyl radicals. This work presents a novel strategy for fabricating lanthanide-based scintillator@MOF nanocomposites for efficient X-PDT and is anticipated to promote theranostic applications of nanocomposites.

Introduction

Nanocomposites, consisting of two or more different types of nanoparticles, are emerging as an important family of artificially multifunctional nanomaterials, as they not only retain the advantageous characteristics of individual components but also exhibit synergistic functions that are absent in neither individual nanoparticles nor their physical mixtures.[1,2] In recent years, nanocomposites have been widely applied in the field of theranostics such as in bioimaging, photodynamic therapy (PDT), and radiotherapy (RT).[3–5] In particular, nanocomposites irradiated by X-ray have been proposed as efficient nanoagents to perform RT and X-ray-induced PDT (X-PDT) on deep-seated tumors, benefiting from the high penetrability and non-invasiveness of X-rays as well as the multiple roles played by nanocomposites.[6,7] To reach the full potential of each component, different synthetic routes have been reported to orderly assemble nanocomposites.[8–14] For example, a theranostic system comprising Ce-doped $LiLuF_4$ and Roussin's black salt was formed by direct coupling *via* electrostatic interactions and has been used for RT sensitization.[15] Polyoxomolybdate and rose bengal as scintillators and photosensitizers were loaded on chitosan to obtain nanocomposites.[16] Nevertheless, the synthesis methods of these nanocomposites are somewhat problematic as direct coupling often suffers from low loading capacity and leakage risk, while the carrier material would reduce the efficiency owing to the increased distance of energy transfer. In addition, scintillators in these nanocomposites also face some drawbacks including weak X-ray attenuation, low luminescence efficiency, and non-adjustable emission wavelengths.

[a]*Key Laboratory of Flexible Electronics (KLOFE) & Institute of Advanced Materials (IAM), Jiangsu National Synergetic Innovation Center for Advanced Materials (SICAM), Nanjing Tech University (NanjingTech), Nanjing, 211816, P.R. China. E-mail: iamqju@njtech.edu.cn*
[b]*State Key Laboratory of Radiation Medicine and Protection, School of Radiation Medicine and Protection and School for Radiological and Interdisciplinary Sciences (RAD-X), Collaborative Innovation Center of Radiation Medicine of Jiangsu Higher Education Institutions, Soochow University, Suzhou, 215123, P.R. China. E-mail: kyang@suda.edu.cn*
[c]*Hospital for Skin Disease, Institute of Dermatology, Chinese Academy of Medical Sciences & Peking Union Medical College, Nanjing, 210042, China*
[d]*Department of Urology, Zhongda Hospital affiliated to Southeast University, Nanjing, 210096, China*

† Electronic supplementary information (ESI) available. See DOI: https://doi.org/10.1039/d3qi02301j

Lanthanides with high atomic numbers, ranging from La (Z = 57) to Lu (Z = 71), endow lanthanide-based/containing materials with a high X-ray attenuation coefficient (*i.e.*, $NaLuF_4$, Kα = 63.31 keV; $NaGdF_4$, Kα = 50.24 keV).[17,18] Meanwhile, ladder-like energy levels of lanthanide ions enable the generation of emission profiles ranging from ultraviolet (UV) to visible (vis) and near-infrared (NIR) through intra-configurational 4f–4f electronic transitions, making them sensitive nanoprobes for X-ray-excited bioimaging and RT.[19,20] In contrast to conventional scintillators, lanthanide-based scintillators not only possess good optical properties (*i.e.*, no photobleaching and blinking) and low toxicity but also have easily modifiable surfaces, facilitating the subsequent construction of multifunctional nanocomposites.[21]

Metal–organic frameworks (MOFs) are highly crystallized porous materials formed by the self-assembly of metal ions/metal clusters as nodes and organic ligands as link units. MOFs show innate structural advantages of structure tailorability, open channel structure, high porosity, and functionalized surface.[22] Importantly, certain photosensitizers such as 5,10,15,20-tetra(*p*-benzoato)bacteriochlorin (TBB) and meso-tetra(4-carboxyphenyl)porphine (TCPP) can be incorporated as organic ligands within the framework, producing more singlet oxygen and averting the self-quenching of molecular photosensitizers caused by aggregation.[23,24] The integration of MOFs constructed using photosensitizers with lanthanide-based scintillators to form nanocomposites allows for the conversion of highly penetrable X-rays into UV-vis radiations, enabling the activation of MOFs to achieve desirable functionalities such as the generation of ROS.[25] Unfortunately, research on lanthanide-based scintillator@MOF nanocomposites is still in its infancy.[26,27]

In this work, we designed a new X-ray-irradiated nanocomposite that combines $NaGdF_4$:Tb @$NaGdF_4$:Ce @$NaLuF_4$ scintillator nanoparticles (SNPs) with Hf-porphyrin (Hf-TCPP) MOFs *via* a surface-assisted epitaxial growth strategy for the first time. In this architecture, Ce^{3+} and Tb^{3+} in appropriate amounts were selected to dope in SNPs with the purpose to boost the emission of SNPs under X-ray irradiation and activate TCPP in MOFs, respectively. The introduction of biocompatible high-Z element Hf and photosensitizer TCPP into MOFs can improve radiation sensitization, and the MOFs serve as photosensitizers of X-PDT. Importantly, the uniform and small-sized SNP@MOF nanocomposites with a core–shell structure facilitate efficient energy transfer from SNPs to MOFs. Under X-ray irradiation, SNP@Hf-TCPP nanocomposites can simultaneously generate a large amount of singlet oxygen ($^1O_2$) and hydroxyl radicals ($^{\bullet}OH$) in the ROS test. Furthermore, the therapeutic potential of SNP@Hf-TCPP nanocomposites was further explored in 4T1 tumour cells, which showed significant therapeutic efficacy under low-dose (2Gy) X-ray irradiation. These findings indicate that our projected nanomaterials, SNP@Hf-TCPP nanocomposites, show potential in X-PDT applications.

Experimental section

Materials

Gadolinium(III) acetate hydrate ($Gd(Ac)_3$, 99.9%), lutetium(III) acetate hydrate ($Lu(Ac)_3$, 99.9%), terbium acetate hydrate ($Tb(Ac)_3$, 99.9%), cerium acetate hydrate ($Ce(Ac)_3$, 99.9%), hafnium(IV) chloride ($HfCl_4$), and methoxypolyethylene glycol amine (PEG, M_w = 5000) were purchased from Sigma-Aldrich. Meso-tetra(4-carboxyphenyl)porphine (TCPP) was purchased from Jinan Henghua and 3,4-dihydroxyhydrocinnamic acid was purchased from Aladdin. Oleic acid (OA, 90%) and 1-octadecene (ODE, 90%) were purchased from Alfa Aesar. Anhydrous NH_4F (≥98%), sodium hydroxide (NaOH), and 1-(3-dimethylaminopropyl)-3-ethylcarbodiimide hydrochloride (EDC) were obtained from Energy Chemical. All chemicals were used as received without further purification.

Synthesis of SNP nanoparticles

The lanthanide-based nanoparticles were synthesized through high-temperature coprecipitation in a binary solvent mixture of OA and ODE.[28] In a typical procedure, 4 mL aqueous solution containing 0.56 mmol $Gd(Ac)_3$ and 0.24 mmol $Tb(Ac)_3$ was mixed with 8 mL OA and 12 mL ODE in a 100 mL three-neck round-bottom flask. The mixture was heated at 115 °C for 60 min to remove water and then heated at 155 °C for 30 min under a nitrogen atmosphere to obtain a Ln-OA chelator, followed by cooling to room temperature. After adding 8.0 mL of methanol solution containing 2.0 mmol NaOH and 3.2 mmol NH_4F, the resultant solution was stirred at 85 °C for 30 min to remove methanol, heated to 280 °C for 1.5 h under a nitrogen atmosphere, and then cooled to room temperature. The resulting nanoparticles were precipitated with ethanol, collected by centrifugation, washed with cyclohexane and ethanol several times, and re-dispersed in 4 mL cyclohexane. The procedures were repeated for layer-by-layer growth of $NaGdF_4$:Tb@$NaGdF_4$:Ce core–shell and/or $NaGdF_4$:Tb@$NaGdF_4$:Ce@$NaLuF_4$ core–shell-shell nanoparticles, except that preformed core and/or core–shell nanoparticles were included in the precursor solution.

Synthesis of dopacid-capped SNPs

50 mg as-prepared OA-capped SNPs dispersed in 2 mL tetrahydrofuran (THF) was introduced to 8 mL THF containing 3,4-dihydroxyhydrocinnamic acid (dopacid, 100 mg). The resulting solution was heated at 50 °C for 3 hours and 200 μL aqueous NaOH (0.2 M) was added after cooling to room temperature. The resulting dopacid-capped SNPs were collected by centrifugation, washed with DMF and ethanol to remove the unconjugated dopacid, and resuspended in DMF for later use.

Synthesis of SNP@Hf-TCPP nanocomposites

A solution of 4.5 mg TCPP in 4 mL DMF and 4 mL ethanol was added dropwise to a solution of 12 mg $HfCl_4$ in 12 mL DMF and 12 mL ethanol under sonication, and then a desired amount of dopacid-capped SNPs was added dropwise. The resulting solution was further sonicated for 2 min before

placing it in a 120 °C oil bath for 5 h. Finally, the product was obtained by centrifugation and washed three times with DMF and ethanol.

Characterizations

Transmission electron microscopy (TEM) was carried out using a Hitachi HT7700. High-resolution TEM (HR-TEM) was performed using a JEOL 2100F at 200 kV. High-angle annular dark field scanning transmission electron microscopy (HAADF-STEM) and elemental mapping were performed using an aberration-corrected TEM (Spectra 300, Themo Fisher Scientific, USA) operating at a voltage of 300 kV. Powder X-ray diffraction (XRD) patterns were recorded using a SmartLab diffractometer (Rigaku, Japan) with Ni-filtered Cu Kα radiation (λ = 0.154 nm). The X-ray excited luminescence spectra were recorded using a spectrofluorometer (FLS980, Edinburgh Instruments) under X-ray irradiation (Mini-X2, Amptek; Au target; tube voltage, 50 kV). Fluorescence spectra and decays were recorded at room temperature using an FLS980 equipped with Edinburgh Instruments. Fourier transform infrared (FTIR) spectra were recorded using a PerkinElmer Spectrum 100 Fourier-transform infrared spectrometer. X-ray photoelectron spectroscopy (XPS) measurements were carried out using a Thermo Fisher ESCALAB 250Xi with Al Kα (1486.6 eV) and He Iα (21.2 eV) as the sources of radiation. The UV-vis absorption spectra were recorded using a SHIMADZU UV-1780. Dynamic light scattering (DLS) and ζ potential were measured using a Nano ZS ZEN3600 system (Malvern). The nanoparticle solution should pass through a 0.2 μm filter before measuring the DLS. The Brunauer–Emmett–Teller (BET) surface areas and pore size distributions, analyzed by both the Barrett–Joyner–Halenda and density functional theory methods, were determined from the isothermal N_2 (99.9999%) adsorption/desorption curves of all samples with a weight of ~100 mg, recorded using a Micromeritics 3 FLEX instrument at 78 K. Time-resolved spectra were recorded using a Cytation 5 (Biotek).

Results and discussion

Synthesis and characterization of SNP@MOF nanocomposites

The synthesis procedure of the nanocomposites is shown in Fig. 1a, where lanthanide-based SNPs with a core–shell–shell structure were synthesized, modified with dopacid, and further used as seeds for the formation of SNP@MOF nanocomposites. In particular, $NaGdF_4$:30 at% Tb nanoparticles with an average diameter of ~8.1 nm (Fig. 1b) were first fabricated as an emissive core *via* a high-temperature co-precipitation method[29] and then used for epitaxially growing a $NaGdF_4$:20 at% Ce shell to enhance X-ray-excited luminescence by constructing an energy transfer route from Ce to Tb. The thickness of the $NaGdF_4$:20 at% Ce shell was measured to be approximately 3.1 nm (Fig. 1c), which can preserve the emission of Tb^{3+} by keeping the surface defects away from the

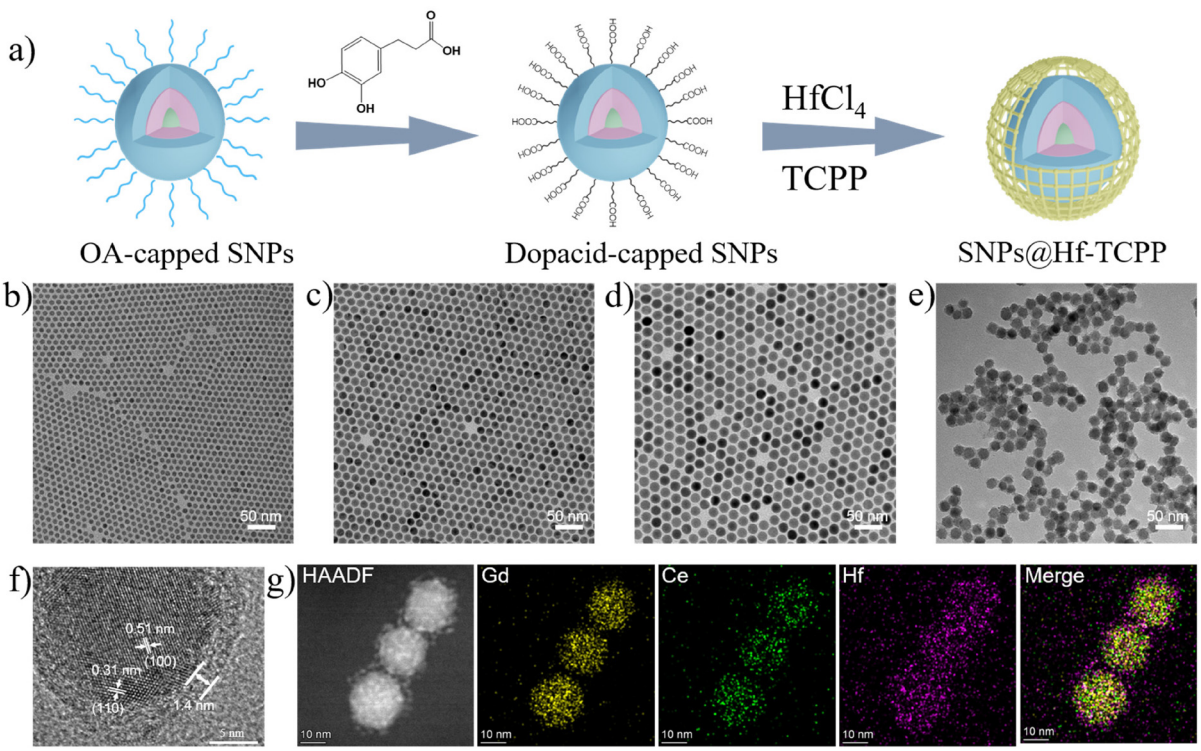

Fig. 1 (a) Schematic illustration of the construction of SNP@Hf-TCPP nanocomposites. TEM images of (b) $NaGdF_4$:Tb, (c) $NaGdF_4$:Tb@$NaGdF_4$:Ce, and (d) $NaGdF_4$:Tb@$NaGdF_4$:Ce@$NaLuF_4$ nanoparticles. (e) TEM image, (f) HR-TEM image, (g) HAADF-STEM image and elemental mapping of SNP@Hf-TCPP nanocomposites.

emissive core. Moreover, an optically inert $NaLuF_4$ shell (2.1 nm) was coated on $NaGdF_4$:30 at% Tb@$NaGdF_4$:20 at% Ce core–shell nanoparticles to further isolate the emissive core away from the quenching surface, resulting in bright emission of Tb^{3+}. The resulting SNPs with a core–shell-shell structure showed an average diameter of ~18.5 nm with a narrow size distribution (Fig. 1d and Fig. S1†). The XRD pattern demonstrated that the as-synthesized nanoparticles were in the hexagonal phase of $NaGdF_4$ (JCPDS 27-0699), and no peak assigned to impurities was detected (Fig. S2†). SNPs were then subjected to ligand exchange by small-molecule carboxylate ligands (*i.e.*, dopacid) for subsequent heterogeneous nucleation and growth of Hf-TCPP MOFs. As shown in the FTIR spectra (Fig. S3†), the original OA-capped SNPs show strong bands peaked at 2926 and 2852 cm^{-1}, assigned to the stretching and rocking vibrations of $-CH_2-$ in OA.[30] After ligand exchange, the stretching vibrations of C=O and C–O located at 1659 and 1250 cm^{-1} are observed, while the $-CH_2-$ peaks significantly decrease, indicating that dopacid successfully substitutes OA and coats the surface of SNPs.

To fabricate SNP@Hf-TCPP core–shell nanocomposites, dopacid-capped SNPs and MOF precursors ($HfCl_4$ and TCPP) were mixed and heated at 120 °C. The representative TEM image of the SNP@Hf-TCPP nanocomposites (Fig. 1e) demonstrates that the obtained nanocomposites are uniform core–shell spheres with a diameter of ~21.3 nm, and the thickness of the Hf-TCPP MOFs was calculated to be ~1.4 nm (Fig. S4†). Owing to the presence of dopacid, the MOF precursor prefers nucleation on the existing carboxylic SNP surface rather than self-nucleation. A similar result was also observed in the formation of UCNP@PCN-224 core–shell nanocomposites, where citric acid having several carboxylic groups was coated onto the UCNPs to assist the growth of PCN-224 around upconversion nanoparticles (UCNPs).[31] Additional evidence for the growth of Hf-TCPP MOFs on a single SNP is provided by the HR-TEM image displayed in Fig. 1f, where the SNP is coated with Hf-TCPP to a thickness of ~1.4 nm and legible lattice fringes are observed with interplanar spacings of 0.51 and 0.31 nm, which are consistent with the (100) and (110) planes of hexagonal $NaGdF_4$, respectively. The powder XRD pattern of SNP@Hf-TCPP nanocomposites (Fig. S5†) shows sharp peaks that correspond to the hexagonal phase of $NaGdF_4$ SNPs, along with peaks assigned to the hexagonal-phase Hf-TCPP MOFs, while no peak assigned to impurities is detected. Further validation of the composition of the core–shell nanocomposites is provided by elemental mapping images acquired using a HAADF-STEM (Fig. 1g). The well-organized core–shell structure was confirmed by HAADF-STEM, and the elemental mapping images undoubtedly demonstrated that Hf was homogeneously distributed throughout the entire nanocomposites, covering a larger area than Gd and Ce, indicating that the SNPs were surrounded by a uniform Hf-TCPP shell.

Besides TEM and XRD results, the ζ potential unambiguously denotes the successful coating of Hf-TCPP on SNPs as it alternated from negative to positive after the growth of Hf-TCPP on SNPs (Fig. 2a). In fact, the positive surface of nanoparticles is anticipated to facilitate their internalization into cells due to the negative charge on the cell surface.[32] As shown in Fig. 2b, the hydration diameter of the obtained SNP@Hf-TCPP nanocomposites was measured to be ~115.7 nm with a polydispersity index (P.I.) of 0.152, demonstrating a favourable colloidal dispersibility of the nanocomposites in an aqueous solution. After dispersion in water for 7 months, the SNP@Hf-TCPP nanocomposites still exhibited a core–shell structure

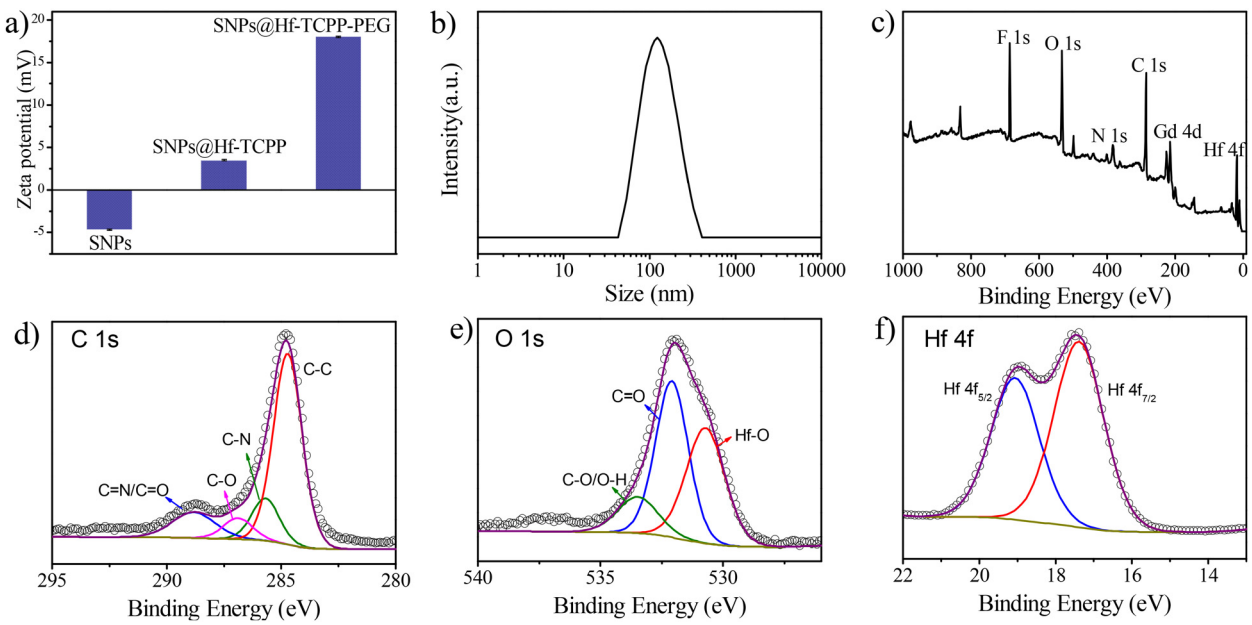

Fig. 2 (a) ζ potential of SNPs, SNP@Hf-TCPP, and SNP@Hf-TCPP-PEG nanocomposites. (b) DLS of SNP@Hf-TCPP nanocomposites in an aqueous solution. (c) XPS spectrum of SNP@Hf-TCPP nanocomposites, and high-resolution XPS spectra of (d) C 1s, (e) O 1s, (f) Hf 4f.

(Fig. S6†). To further investigate the surface chemical structure of the nanocomposites, XPS with high-resolution analysis was carried out (Fig. 2c–f). The C 1s signals were located at approximately 284.8, 285.8, 286.9, and 288.7 eV, which could be ascribed to C–C, C–N, C–O, and C═N/C═O of TCPP, respectively. The O 1s signals were located near 530.7, 532.1, and 533.5 eV, corresponding to Hf–O, C═O, and C–O/O–H of TCPP, respectively. In addition, the signals of C–O/O–H were much lower than those of C═O, indicating the successful coordination of Hf^{4+} with the carboxylic group originating from TCPP. The Hf 4f signals at 17.4 and 19.1 eV were primarily attributed to the transitions of Hf $4f_{7/2}$ and Hf $4f_{5/2}$, respectively. As the presence of pores in MOFs is anticipated to significantly affect the mass exchange rate and the diffusion of produced ROS, the N_2 adsorption–desorption isotherms of the nanocomposites were measured (Fig. S7†). SNP@MOF nanocomposites exhibited a typical type IV adsorption N_2 isotherm with mesoporous structure characteristics, originating from Hf-TCPP. The BET surface area of the SNP@Hf-TCPP nanocomposites was 49.04 $cm^3\ g^{-1}$, and the average sizes of the pores were 1.47 and 3.15 nm, respectively, according to the pore size distribution measurement.

Optical properties of the SNP@MOF nanocomposites

Although $NaLuF_4$ exhibits a stronger X-ray absorption coefficient than that of $NaGdF_4$ ($NaLuF_4$, Kα = 63.31 keV; $NaGdF_4$, Kα = 50.24 keV), it tends to enhance the afterglow intensity of Tb^{3+}, reducing the intensity of fast spontaneous emission.[17] As a result, $NaGdF_4$ other than $NaLuF_4$ was selected as the primary matrix for the emissive core of the SNPs. The proposed energy transfer mechanism of the SNP@Hf-TCPP nanocomposites is shown in Fig. 3a. For SNPs under the excitation of X-ray, large amounts of electrons with different energies are generated, and the ground state of Ce^{3+} and Gd^{3+} absorbs the energy of secondary electrons to an excited state, which can further transfer their energy to nearby Tb^{3+} to produce strong green luminescence. Although Tb^{3+} can also absorb the energy of one secondary electron to the excited state by itself, the presence of Lu^{3+}, Ce^{3+}, and Gd^{3+} in $NaLnF_4$ is anticipated to enhance the absorption and conversion of X-ray energy, accompanied by more pathways constructed with Ce^{3+} and Gd^{3+} for transferring energy to Tb^{3+} to boost the emission intensity of SNPs. After epitaxial growth of MOFs around SNPs, TCPP in the outer Hf-TCPP shell can be excited by the energy transferred from Tb^{3+} to enable the generation of $^1O_2$. The well-organized core–shell structure of the SNP@Hf-TCPP nanocomposites facilitates the reduction of the distance between the activator Tb^{3+} and the photosensitizer TCPP, maximizing the energy transfer efficacy. X-ray excited fluorescence (XEF) spectra revealed that SNPs exhibited strong green emission with four main peaks located at 490, 545, 585, and 621 nm, which corresponded to $^5D_4$ to ^7F_J (J = 6, 5, 4, and 3) transitions of Tb^{3+}, respectively (Fig. 3b and Fig. S9†). Besides these four main bands, three weak peaks centered at 648, 667, and 679 nm, which were attributed to the transitions from $^5D_4$ to ^7F_J (J = 2, 1, and 0) of Tb^{3+}, as well as the emission band peaked at 311 nm, which was assigned to the transition of

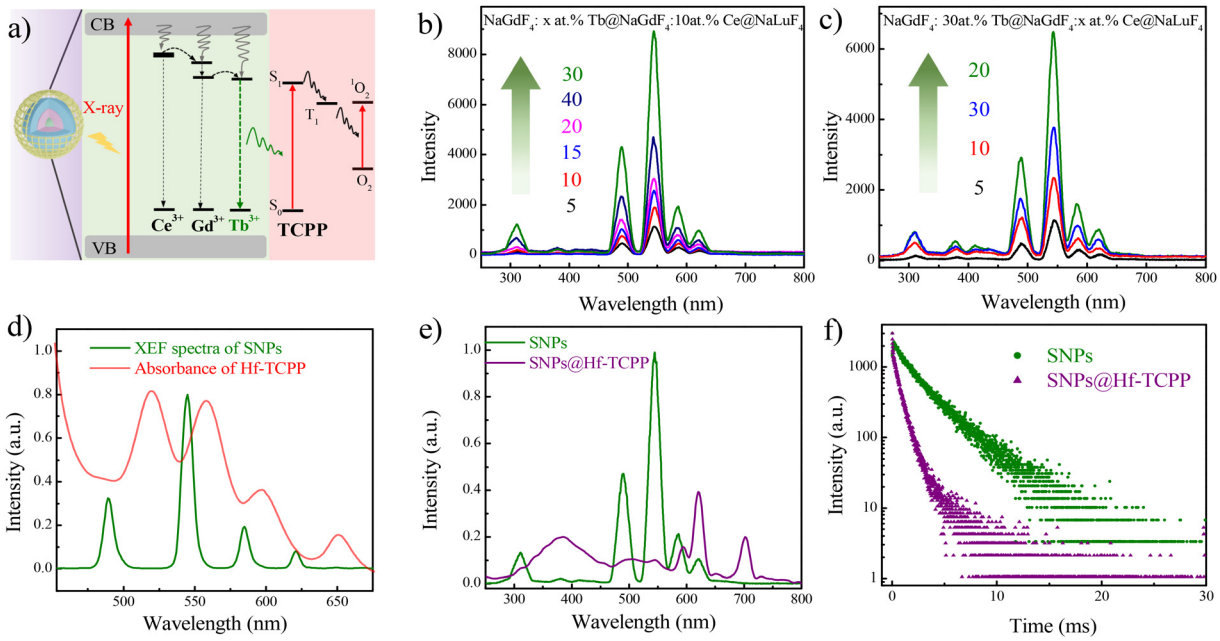

Fig. 3 (a) Schematic illustration of the energy transfer mechanism of SNP@MOF nanocomposites. (b and c) X-ray excited fluorescence spectra of SNPs with different Tb^{3+} and Ce^{3+} doping concentrations. (d) XEF spectra of SNPs and absorption spectra of Hf-TCPP. (e) Emission spectra of SNPs and SNP@Hf-TCPP under X-ray irradiation. (f) Fluorescence delay curves of SNPs and SNP@Hf-TCPP monitored at 545 nm at an excitation wavelength of 254 nm.

Gd^{3+}, were observed, indicating that the applied SNPs belong to a good optical host. When UV light was used as the excitation source instead of X-ray, a similar emission spectrum was obtained (Fig. S8†).

To achieve the strongest emission of Tb in SNPs, the optimal doping concentrations of the emitter (Tb^{3+}) and sensitizer (Ce^{3+}) in SNPs were investigated using XEF spectra. As shown in Fig. 3b, the emission intensity gradually increases as the doping concentration of the activator Tb^{3+} increases from 5 to 30 at%. However, the XEF intensity decreases when the doping concentration of Tb^{3+} is 40 at%, which may be induced by the concentration quenching effect. Thus, the optimal doping concentration of Tb^{3+} was set to 30 at%. For $NaGdF_4$:30 at% Tb@$NaGdF_4$:*x* at.%Ce@$NaLuF_4$ SNPs, the emission intensity first increases as the doping concentration of Ce^{3+} increases from 5 to 20 at%, and then decreases as it increases from 20 to 30 at%, showing a similar trend to that of Tb and further indicating that the optimal doping concentration of Ce^{3+} is 20 at% (Fig. 3c). Therefore, $NaGdF_4$:30 at% Tb@$NaGdF_4$:20 at%Ce@$NaLuF_4$ core–shell-shell nanoparticles are used as SNPs for the subsequent growth of MOFs.

The XEF spectra of SNP exhibit good overlap with the absorption of Hf-TCPP (Fig. 3d), implying that it is possible to efficiently activate TCPP through the emission of Tb^{3+}. After epitaxial growth of Hf-TCPP MOFs, three emission bands of Tb^{3+} peaked at 490, 545, and 585 nm dropped to near zero, while a new band peaked at 702 nm appeared, which could be attributed to the characteristic emission of TCPP (Fig. S9†). To exclude the emission of Hf-TCPP under X-ray irradiation, the XEF of Hf-TCPP was measured, and no emission was observed (Fig. S10†). These results unambiguously indicate that the emission of Tb^{3+} is efficiently used to activate TCPP through resonant and/or nonresonant energy transfer from the inner SNP to the outer Hf-TCPP shell. Besides, a broad band centered at 385 nm was observed in SNP@Hf-TCPP nanocomposites, which may be attributed to the emission of surface-capped dopacid. A similar broad emission band was observed in the emission spectra of dopacid-capped SNPs under the excitation of X-ray, confirming that this emission band originates from the surface-capped dopacid (Fig. S11†). To further confirm whether TCPP is activated by the resonant or nonresonant energy transfer from Tb^{3+}, the decay curves of SNPs and SNP@Hf-TCPP nanocomposites (Fig. 3f) as well as the time-resolved emission spectra of SNP@Hf-TCPP nanocomposites (Fig. S12†) were measured, respectively. After the epitaxial growth of Hf-TCPP on SNPs, the lifetime of Tb^{3+} at 545 nm decreased significantly from 2.41 ms to 0.55 ms, indicating the occurrence of resonant energy transfer between Tb and TCPP. The energy transfer efficiency can be calculated as $1-\tau_{DA}/\tau_D$, where τ_{DA} and τ_D are the fluorescence lifetimes of the SNP donor with and without the energy acceptor, respectively. The results indicated that the energy transfer efficiency from the SNP cores to the shells of the SNP@Hf-TCPP nanocomposites was ~77%. However, the TCPP emission peak is weaker in the time-resolved spectra under an excitation of 254 nm with the delay time and gate time set to 20 μs and 1 ms, respectively, indicating that the strong emission band of TCPP in the XEF spectra should be mainly assigned to the reabsorption of Tb^{3+}. These results indicate that benefiting from the intact core–shell structure of SNP@Hf-TCPP nanocomposites, TCPP can be activated by both resonant and nonresonant energy transfer from Tb^{3+} to TCPP, facilitating their application in X-PDT.

X-ray-induced ROS generation

Prior to investigating the specific types of X-ray-induced ROS, a preliminary study on the ROS generation of SNP@Hf-TCPP nanocomposites under X-ray irradiation was conducted, where 1,3-diphenylisobenzofuran (DPBF) was used as an indicator to evaluate the ROS generation capacity.[33] As shown in Fig. 4a, the absorption intensity of DPBF at 410 nm gradually decreases with the increase in irradiation dose from 0 to 10 Gy. Normalizing the initial absorption value of DPBF before irradiation, SNP@Hf-TCPP nanocomposites exhibited an approximately 60% decrease in absorption intensity after 10 Gy (Fig. 4b), demonstrating their remarkable ROS generation capability. Subsequently, to investigate the generation of ROS under X-ray irradiation at different doses, singlet oxygen sensor green (SOSG) and 3,3′,5,5′-tetramethylbenzidine (TMB) were employed as trapping agents for $^1O_2$ and $^{\bullet}OH$, respectively. As shown in Fig. 4c, a significant enhancement of the fluorescence of SOSG at 525 nm was observed for SNP@Hf-TCPP nanocomposites as the irradiation dose increased from 0 to 10 Gy. Particularly, under a low radiation dose of 2 Gy, the fluorescence intensity of SOSG in the SNP@Hf-TCPP rapidly increased, indicating remarkable $^1O_2$ generation capability. Interestingly, $^1O_2$ was also generated in SNPs under the irradiation of X-ray, indicating that SNPs can also serve as X-ray photosensitizers despite their low efficacy.[34] High-Z heavy atoms such as Gd, Lu, and Hf incorporated into the nanocomposites are anticipated to play a crucial role in enhancing radiation sensitization by producing highly energetic electrons due to their larger atomic nuclei. These high-energy electrons can interact with water molecules, leading to the ionization of water and the formation of $^{\bullet}OH$ through the process of "radiolysis of water".[35] This is evidenced by a significant increase in the absorption intensity of TMB in SNP@Hf-TCPP with the increase in X-ray irradiation dose (Fig. 4d). It should be noted that although SNPs also exhibit a similar trend, the introduction of an Hf-TCPP shell around SNPs substantially boosts the generation of $^{\bullet}OH$, resulting in improved RT efficacy.

To enhance biocompatibility and prolong circulation half-life, all samples were PEGylated in the following related cell experiments. After the modification of PEG, the ζ potential of the SNP@Hf-TCPP-PEG nanocomposites increased significantly from 3.52 to 18.03 mV (Fig. 2a). The cellular uptake of SNP@Hf-TCPP nanocomposites was evaluated using confocal fluorescence imaging (Fig. S13†), where a red fluorescence signal belonging to TCPP was observed in GL216 cells cultured with SNP@Hf-TCPP nanocomposites at 37 °C for 3 h,

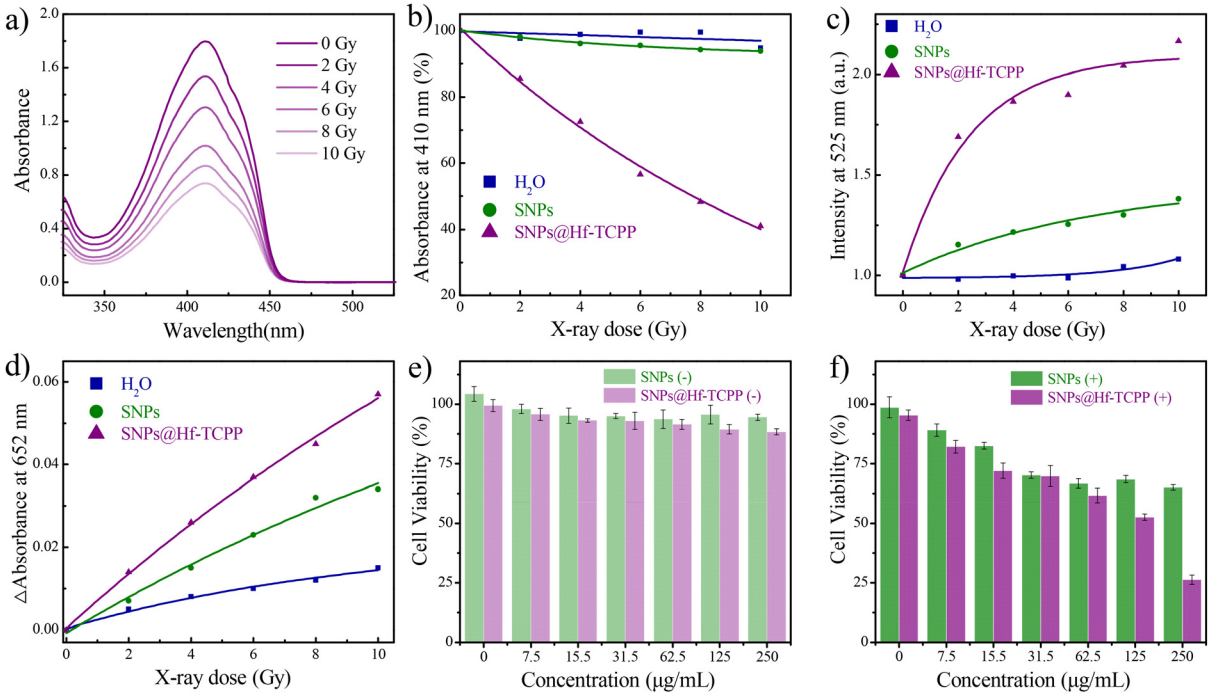

Fig. 4 (a) UV–vis absorbance curves of DPBF with SNP@Hf-TCPP nanocomposites under X-ray irradiation at different doses. (b) Normalized absorbance intensity of DPBF containing H_2O, SNPs, and SNP@Hf-TCPP nanocomposite. (c) Generation of $^1O_2$ determined by SOSG fluorescence intensity under X-ray irradiation at different doses. (d) Generation of $^{\bullet}OH$ detected by TMB as a trapping agent under X-ray irradiation at different doses. (e and f) Cell viability of 4T1 cells treated with different concentrations of SNPs and SNP@Hf-TCPP nanocomposites without or with X-ray irradiation (2 Gy), respectively.

indicating efficient cellular internalization. Encouraged by the promising ROS production observed in SNP@Hf-TCPP nanocomposites under X-ray irradiation, further exploration of their potential application in cancer therapy was conducted *via in vitro* experiments. Before analysing the therapy performance, the cytotoxicity of the nanocomposites was evaluated. As shown in Fig. 4e, the 4T1 cells exhibited a high survival rate (>90%) after treatment with different concentrations of SNPs and SNP@Hf-TCPP nanocomposites (0–250 μg mL^{-1}) for 24 h, demonstrating the low cytotoxicity and high biocompatibility of SNPs and SNP@Hf-TCPP nanocomposites. Under 2 Gy X-ray irradiation, the cellular viability of SNP@Hf-TCPP nanocomposites was markedly reduced, which was attributed to the effective ROS generation through enhanced $^1O_2$-associated X-PDT and $^{\bullet}OH$-associated RT. When the concentration of SNP@Hf-TCPP nanocomposites was 250 μg mL^{-1}, more than 75% of cells died, indicating the high efficacy of nanocomposites in X-induced therapy. Under the same measurement conditions, SNP@HfTCPP nanocomposites exhibited similar X-PDT efficacy to previously reported polyoxomolybdate nanoclusters loaded with the rose bengal nanosystem.[16] In contrast, in the control SNP group (250 μg mL^{-1}), a higher cell survival rate (65%) was observed (Fig. 4f), unambiguously indicating that SNP@Hf-TCPP nanocomposites are more efficient in cancer therapy.

Conclusions

In summary, X-ray-activated nanocomposites based on lanthanide-based scintillator nanoparticles and Hf-porphyrinic MOFs have been proposed and synthesized for X-ray-induced photodynamic therapy. Benefiting from the surface-capped dopacid ligand, uniform and small-sized SNP@Hf-TCPP nanocomposites with a core–shell nanostructure were formed through epitaxial growth. Owing to the efficient energy transfer from radioluminescent SNPs, the outer shell of Hf-TCPP can be activated to produce singlet oxygen under the irradiation of X-ray. Meanwhile, the presence of high Z elements (Gd, Lu, Tb, Ce, and Hf) in nanocomposites can substantially enhance radiation sensitization, promoting the generation of hydroxyl radicals. In the *in vitro* 4T1 cell experiments, the nanocomposites demonstrated remarkable therapeutic efficacy, where more than 75% of cells died under low dose (2 Gy). We are convinced that SNP@Hf-TCPP nanocomposites hold promising potential for cancer treatment, particularly as X-PDT agents and radiation sensitizers to enhance therapeutic efficacy.

Conflicts of interest

There are no conflicts to declare.

Acknowledgements

This work was financially supported by the National Natural Science Foundation of China (22375090, 21975122, and 21871139).

References

1 Q. Liu, B. Wu, M. Li, Y. Huang and L. Li, Heterostructures Made of Upconversion Nanoparticles and Metal-Organic Frameworks for Biomedical Applications, *Adv. Sci.*, 2021, **9**(3), 2103911.
2 J. Du, T. Jia, J. Zhang and G. Chen, Heterostructures Combining Upconversion Nanoparticles and Metal-Organic Framework: Fundamental, Classification, and Theranostic Applications, *Adv. Opt. Mater.*, 2023, **11**(11), 2202122.
3 H. Chen, G. D. Wang, Y. Chuang, Z. Zhen, X. Chen, P. Biddinger, Z. Hao, F. Liu, B. Shen, Z. Pan and J. Xie, Nanoscintillator-Mediated X-ray Inducible Photodynamic Therapy for In Vivo Cancer Treatment, *Nano Lett.*, 2015, **15**(4), 2249–2256.
4 X. Chen, J. Song, X. Chen and H. Yang, X-ray-Activated Nanosystems for Theranostic Applications, *Chem. Soc. Rev.*, 2019, **48**(11), 3073–3101.
5 L. He, Q. Ni, J. Mu, W. Fan, L. Liu, Z. Wang, L. Li, W. Tang, Y. Liu, Y. Cheng, L. Tang, Z. Yang, Y. Liu, J. Zou, W. Yang, O. Jacobson, F. Zhang, P. Huang and X. Chen, Solvent-Assisted Self-Assembly of a Metal–Organic Framework Based Biocatalyst for Cascade Reaction Driven Photodynamic Therapy, *J. Am. Chem. Soc.*, 2020, **142**(14), 6822–6832.
6 A. J. J. M. van Breemen, M. Simon, O. Tousignant, S. Shanmugam, J.-L. van der Steen, H. B. Akkerman, A. Kronemeijer, W. Ruetten, R. Raaijmakers, L. Alving, J. Jacobs, P. E. Malinowski, F. De Roose and G. H. Gelinck, Curved Digital X-ray Detectors, *npj Flexible Electron.*, 2020, **4**(1), 22.
7 H. Wang, B. Lv, Z. Tang, M. Zhang, W. Ge, Y. Liu, X. He, K. Zhao, X. Zheng, M. He and W. Bu, Scintillator-Based Nanohybrids with Sacrificial Electron Prodrug for Enhanced X-ray-Induced Photodynamic Therapy, *Nano Lett.*, 2018, **18**(9), 5768–5774.
8 C. Hsu, S. Lin and C. A. Chang, Lanthanide-Doped Core-Shell-Shell Nanocomposite for Dual Photodynamic Therapy and Luminescence Imaging by a Single X-ray Excitation Source, *ACS Appl. Mater. Interfaces*, 2018, **10**(9), 7859–7870.
9 W. Fan, W. Bu, Z. Zhang, B. Shen, H. Zhang, Q. He, D. Ni, Z. Cui, K. Zhao, J. Bu, J. Du, J. Liu and J. Shi, X-ray Radiation-Controlled NO-Release for On-Demand Depth-Independent Hypoxic Radiosensitization, *Angew. Chem., Int. Ed.*, 2015, **54**(47), 14026–14030.
10 W. Park, S. Cho, D. Kang, J. H. Han, J. H. Park, B. Lee, J. Lee and D. H. Kim, Tumor Microenvironment Targeting Nano-Bio Emulsion for Synergistic Combinational X-ray PDT with Oncolytic Bacteria Therapy, *Adv. Healthcare Mater.*, 2020, **9**(13), 1901812.
11 W. Zhang, X. Zhang, Y. Shen, F. Shi, C. Song, T. Liu, P. Gao, B. Lan, M. Liu, S. Wang, L. Fan and H. Lu, Ultra-High FRET Efficiency $NaGdF_4$:Tb^{3+}-Rose Bengal Biocompatible Nanocomposite for X-ray Excited Photodynamic Therapy Application, *Biomaterials*, 2018, **184**, 31–40.
12 Y. Li, M. Jiang, Z. Deng, S. Zeng and J. Hao, Low Dose Soft X-ray Remotely Triggered Lanthanide Nanovaccine for Deep Tissue CO Gas Release and Activation of Systemic Anti–Tumor Immunoresponse, *Adv. Sci.*, 2021, **8**(12), 2004391.
13 F. Ahmad, X. Wang, Z. Jiang, X. Yu, X. Liu, R. Mao, X. Chen and W. Li, Codoping Enhanced Radioluminescence of Nanoscintillators for X-ray-Activated Synergistic Cancer Therapy and Prognosis Using Metabolomics, *ACS Nano*, 2019, **13**(9), 10419–10433.
14 Z. Du, X. Wang, X. Zhang, Z. Gu, X. Fu, S. Gan, T. Fu, S. Xie and W. Tan, X–Ray–triggered Carbon Monoxide and Manganese Dioxide Generation based on Scintillating Nanoparticles for Cascade Cancer Radiosensitization, *Angew. Chem., Int. Ed.*, 2023, **62**(23), e202302525.
15 Z. Du, X. Zhang, Z. Guo, J. Xie, X. Dong, S. Zhu, J. Du, Z. Gu and Y. Zhao, X-ray-Controlled Generation of Peroxynitrite Based on Nanosized $LiLuF_4$:Ce^{3+} Scintillators and their Applications for Radiosensitization, *Adv. Mater.*, 2018, **30**(43), 1804046.
16 D. Maiti, J. Zhong, Z. Zhang, H. Zhou, S. Xion, Z. Dong, S. Kumar, Z. Liu and K. Yang, Polyoxomolybdate (POM) Nanoclusters with Radiosensitizing and Scintillating Properties for Low Dose X-ray Inducible Radiation-Radiodynamic Therapy, *Nanoscale Horiz.*, 2020, **5**(1), 109–118.
17 X. Ou, X. Qin, B. Huang, J. Zan, Q. Wu, Z. Hong, L. Xie, H. Bian, Z. Yi, X. Chen, Y. Wu, X. Song, J. Li, Q. Chen, H. Yang and X. Liu, High-Resolution X-ray Luminescence Extension Imaging, *Nature*, 2021, **590**(7846), 410–415.
18 L. Lei, Y. Wang, W. Xu, R. Ye, Y. Hua, D. Deng, L. Chen, P. N. Prasad and S. Xu, Manipulation of Time-Dependent Multicolour Evolution of X-ray Excited Afterglow in Lanthanide-Doped Fluoride Nanoparticles, *Nat. Commun.*, 2022, **13**(1), 5739.
19 J. Yan, B. Li, P. Yang, J. Lin and Y. Dai, Progress in Light–Responsive Lanthanide Nanoparticles toward Deep Tumor Theranostics, *Adv. Funct. Mater.*, 2021, **31**(42), 2104325.
20 K. Yang, Y. Yang, D. Sun, S. Li, X. Song and H. Yang, Designing highly UV-emitting lanthanide nanoscintillators for in vivo X-ray-activated tumor therapy, *Sci. China Mater.*, 2023, **66**(10), 4090–4099.
21 L. Lei, Y. Wang, A. Kuzmin, Y. Hua, J. Zhao, S. Xu and P. N. Prasad, Next generation lanthanide doped nanoscintillators and photon converters, *eLight*, 2022, **2**(1), 17.
22 A. Kirchon, L. Feng, H. F. Drake, E. A. Joseph and H. Zhou, From Fundamentals to Applications: a Toolbox for Robust and Multifunctional MOF Materials, *Chem. Soc. Rev.*, 2018, **47**(23), 8611–8638.

23 T. Luo, K. Ni, A. Culbert, G. Lan, Z. Li, X. Jiang, M. Kaufmann and W. Lin, Nanoscale Metal–Organic Frameworks Stabilize Bacteriochlorins for Type I and Type II Photodynamic Therapy, *J. Am. Chem. Soc.*, 2020, **142**(16), 7334–7339.

24 J. Park, Q. Jiang, D. Feng, L. Mao and H. Zhou, Size-Controlled Synthesis of Porphyrinic Metal-Organic Framework and Functionalization for Targeted Photodynamic Therapy, *J. Am. Chem. Soc.*, 2016, **138**(10), 3518–3525.

25 L. Zhang, M. Liu, Z. Fang and Q. Ju, Synthesis and Biomedical Application of Nanocomposites Integrating Metal-Organic Frameworks with Upconversion Nanoparticles, *Coord. Chem. Rev.*, 2022, **468**, 214641.

26 X. Zhao, Y. Li, L. Du, Z. Deng, M. Jiang and S. Zeng, Soft X–Ray Stimulated Lanthanide@MOF Nanoprobe for Amplifying Deep Tissue Synergistic Photodynamic and Antitumor Immunotherapy, *Adv. Healthcare Mater.*, 2021, **10**(21), 2101174.

27 W. Xu, L. Lei, Y. Wang, P. N. Prasad, L. Chen and S. Xu, Spectral Manipulation of X–Ray Excited Optical/Persistent Luminescence by Constructing Metal-Organic Framework@Fluoride Nanoparticles Composites, *Laser Photonics Rev.*, 2023, **17**(5), 2200997.

28 X. Pan, J. Ren, J. Zeng, M. Liu, Z. Fang and Q. Ju, Unravelling Phase and Morphology Evolution of $NaYbF_4$ Upconversion Nanoparticles via Modulating Reaction Parameters, *Inorg. Chem. Front.*, 2022, **9**(16), 4081–4090.

29 Q. Ju, S. Luo, C. Chen, Z. Fang, S. Gao, G. Chen, X. Chen and N. Gu, Single-Irradiation Simultaneous Dual-Modal Bioimaging Using Nanostructure Scintillators as Single Contrast Agent, *Adv. Healthcare Mater.*, 2019, **8**(9), 1801324.

30 M. Slaný, Ľ. Jankovič and J. Madejová, Structural Characterization of Organo-Montmorillonites Prepared From a Series of Primary Alkylamines Salts: Mid-IR and Near-IR Study, *Appl. Clay Sci.*, 2019, **176**, 11–20.

31 Y. Shao, B. Liu, Z. Di, G. Zhang, L. Sun, L. Li and C. Yan, Engineering of Upconverted Metal-Organic Frameworks for Near-Infrared Light-Triggered Combinational Photodynamic/Chemo-/Immunotherapy against Hypoxic Tumors, *J. Am. Chem. Soc.*, 2020, **142**(8), 3939–3946.

32 A. Asati, S. Santra, C. Kaittanis and J. M. Perez, Surface-Charge-Dependent Cell Localization and Cytotoxicity of Cerium Oxide Nanoparticles, *ACS Nano*, 2010, **4**(9), 5321–5331.

33 C. Yang, M. Wang, M. Chang, M. Yuan, W. Zhang, J. Tan, B. Ding, P. Ma and J. Lin, Heterostructural Nanoadjuvant CuSe/$CoSe_2$ for Potentiating Ferroptosis and Photoimmunotherapy through Intratumoral Blocked Lactate Efflux, *J. Am. Chem. Soc.*, 2023, **145**(13), 7205–7217.

34 X. Zhong, X. Wang, G. Zhan, Y. Tang, Y. Yao, Z. Dong, L. Hou, H. Zhao, S. Zeng, J. Hu, L. Cheng and X. Yang, $NaCeF_4$:Gd,Tb Scintillator as an X-ray Responsive Photosensitizer for Multimodal Imaging-Guided Synchronous Radio/Radiodynamic Therapy, *Nano Lett.*, 2019, **19**(11), 8234–8244.

35 Z. H. Loh, G. Doumy, C. Arnold, L. Kjellsson, S. H. Southworth, A. Al Haddad, Y. Kumagai, M. F. Tu, P. J. Ho, A. M. March, R. D. Schaller, M. S. B. Yusof, T. Debnath, M. Simon, R. Welsch, L. Inhester, K. Khalili, K. Nanda, A. I. Krylov, S. Moeller, G. Coslovich, J. Koralek, M. P. Minitti, W. F. Schlotter, J. E. Rubensson, R. Santra and L. Young, Observation of The Fastest Chemical Processes in The Radiolysis of Water, *Science*, 2020, **367**(6474), 179–182.